Microstructure-electrochemical behavior relationship in post processed AISI316L stainless steel parts fabricated by laser powder bed fusion

Available online at www.sciencedirect.com

jmr&t Journal of Materials Research and Technology

journal homepage: www.elsevier.com/locate/jmrt

Original Article

Microstructure-electrochemical behavior relationship in post processed AISI316L stainless steel parts fabricated by laser powder bed fusion

Amir Behjat [a,b], *Morteza Shamanian* [a], *Aboozar Taherizadeh* [a], *Erika Lannunziata* [b], *Sara Bagherifard* [c], *Elżbieta Gadalińska* [d], *Abdollah Saboori* [b,*], *Luca Iuliano* [b]

[a] *Department of Materials Engineering, Isfahan University of Technology, Isfahan, Iran*
[b] *Integrated Additive Manufacturing Center, Department Management and Production Engineering, Politecnico di Torino, Torino, Italy*
[c] *Department of Mechanical Engineering, Politecnico di Milano, Milano, Italy*
[d] *Łukasiewicz Research Network – Institute of Aviation, Materials and Structures Research Center, Al. Krakowska 110/114, 02-256, Warszawa, Poland*

ARTICLE INFO

Article history:
Received 9 December 2022
Accepted 31 January 2023
Available online 6 February 2023

Keywords:
Additive manufacturing
Laser powder bed fusion
Surface post-treatment
Crystal defect
Pitting corrosion
Polarization resistance

ABSTRACT

AISI316L stainless steel components produced via additive manufacturing techniques have quickly found new applications across several industrial sectors. However, parts manufactured through this method generally exhibit poor surface quality and performance in the as-built state. This work addresses the influence of laser polishing and water jet assisted recirculating shot peening on the surface quality, microstructure and electrochemical properties of AISI316L samples produced by the laser powder bed fusion method. To do so, surface roughness analysis, residual stress measurement, scanning electron microscope and electron backscatter diffraction analysis were employed along with electrochemical tests, including cyclic potentiodynamic polarization, electrochemical impedance spectroscopy and Mott-Schottky analysis. Laser polished samples exhibited a smooth surface with high tensile residual stress on the surface, which led to the reduction of pitting potential and formation of passive layers, including more crystal defects. Microscopical analysis evidenced that the higher density of lattice defects and local microstrain on the surface of the shot peened samples promoted surface hardness and induced compressive residual stress. Therfore, the shot peened samples exhibited a wider passive range in cyclic potentiodynamic polarization measurements, higher polarization resistance in electrochemical impedance spectroscopy measurements, and less defective passive film in Mott-Schottky analysis. Moreover, it was calculated that the passive film thickness of the shot peened sample was slightly larger than the other samples. Low surface roughness, high crystal defect density, and compressive residual stresses

* Corresponding author.
E-mail address: abdollah.saboori@polito.it (A. Saboori).
https://doi.org/10.1016/j.jmrt.2023.01.229

enhanced the passive layer's resistance to defect transport, lowered the point defect concentration in the passive film, and improved the pitting resistance of the samples.

1. Introduction

Additive Manufacturing (AM) technique has grown exponentially in development and application thanks to its capability to build complex design objects [1,2]. Recently, AM has emerged as a mainstream means of producing near-net-shaped metallic components from a variety of metallic alloys with minimal waste and post-machining requirements [3,4]. Metal AM processes are primarily divided into two categories: powder bed fusion (PBF) processes, where a spread powder bed is fused via applying predefined laser or electron beam patterns. This includes laser powder bed fusion (L-PBF) and electron beam powder bed fusion (EB-PBF) [5,6]. The second category is directed energy deposition (DED), in which both the material and energy are supplied simultaneously to fabricate a vast range of metallic alloys [7–9]. It is worth mentioning that the final properties of metal AM are a function of the processing parameters. In General, the AM process variables govern the nature of the microstructure and defects formed in the as-built metallic parts [10–12]. Moreover, in some cases, a post-fabrication heat treatment may be requested to eliminate the defects and improve the service performance of the AM parts [13,14].

Due to their outstanding corrosion resistance and desirable mechanical performance, stainless steels are among the most widely researched alloys in the metal AM research field [15,16]. Austenitic grades of stainless steel have been the subject of many research and publications, with AISI316L being one of the most commonly utilized engineering alloys in industrial applications [11,17–20].

Research on the corrosion characteristics of AM stainless steels under various service conditions has increased over the last few years. As reported by several researchers, the pitting corrosion resistance of high-density AM austenitic stainless steel is substantially higher than conventionally produced counterparts [21–23]. Nevertheless, AM components generally exhibit inadequate surface quality in the as-built state [24]. In addition, significant temperature gradients during rapid solidification of the layers may lead to undesired residual stresses [25,26]. Furthermore, different metallurgical, physical and mechanical factors such as microstructure [27,28], distribution of constituent phases and solute segregation [14,17,22], porosity [17], inclusions [29–31], residual stress [32–34] and surface roughness [21,35,36] can significantly affect the corrosion and mechanical behavior of metal AM parts.

In general, a number of solutions including parameter optimization [11,37,38], preheating the feedstock and substrate material [23], post annealing and applying severe plastic deformation (SPD) [23,39–42] were implemented to mitigate the issues caused by microstructural characteristics in AM stainless steels regarding their electrochemical performance.

In recent years, much attention has been devoted to surface modification of AM products via post-treatment [43–47]. Understanding and controlling the surface features using post-treatments is a nascent field with little progress to date for metal AM parts in a wide range of applications. However, up to date, far too little attention has been paid on the quantitative relationship between post-processing surface treatment features and corrosion properties of L-PBF AISI316L.

Hence, in this work, the aim is to quantitatively investigate, for the first time, the relationship between surface integrities and electrochemical behavior of AM AISI316L parts treated by laser polishing as a thermal surface treatment and shot peening as a mechanical surface treatment. The treated and untreated AM samples will be analyzed and compared through different characterization methods, such as 3-D

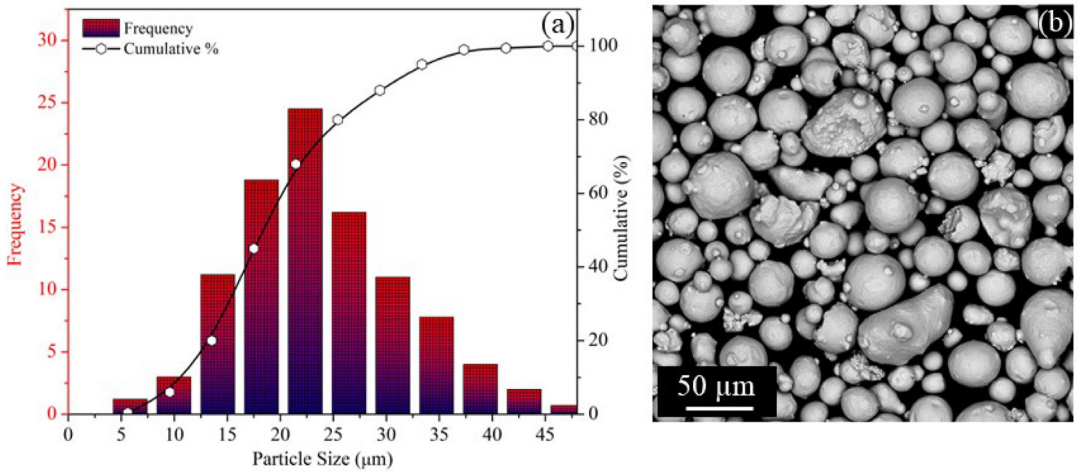

Fig. 1 – (a) Particle size distribution histograms, (b) SEM micrograph of the initial AISI316L powder.

Table 1 – Nominal chemical composition of both the AISI316L wrought sample and the powder feedstock utilized in this study.

Elements	Cr	Ni	Mo	C	Mn	Si	P	S	Fe
Wrought (wt.%)	16~18	10~14	2.0~3.0	0.03	2.0	0.5	0.025	0.01	Bal.
Powder (wt.%)	17.72	13.50	2.04	0.02	2.21	0.48	0.022	0.01	Bal.

profilometry, residual stress measurements, scanning electron microscopy, and corrosion tests.

2. Materials and methods

2.1. Sample preparation

Gas-atomized AISI316L spherical powder (ECKART TLS Gmbh, Germany) with an average size of 27 mm and size distribution of 15–50 mm was used as the feedstock materail. Fig. 1 shows the morphology and particle size distribution (d_{10} = 12.5 μm, d_{50} = 20 μm, d_{90} = 32.5 μm) of the initial powder. Wrought material were used as reference samples for comparative study. The chemical compositions of both wrought and powder AISI316L are presented in Table 1.

Cylindrical samples with a diameter of 12 mm and height of 4 mm were built using a Concept-Laser Mlab-cusing-R system equipped with a 100 Wfiber laser having a beam spot size of 50 μm. A laser power of 95 W, a laser scan speed of 500 mm/s, and hatching distance of 100 μm were used as the standard parameters to produce the L-PBF samples. Before the L-PBF process, the building chamber was purged with argon gas to maintain the oxygen content of the chamber lower than 0.2% throughout the building operation. The schematic of the manufacturing process is shown in Fig. 2(a). The parts were then cut off from the building platform using a wire electric discharge machine (WEDM). The density evaluation of the samples following the Archimedes method verified that all the samples in the as-built state had a relative density of more than 99.5%.

2.2. Post-processing treatments

Laser polishing and recirculating shot peening accelerated by a water jet were used to improve the surface quality of the L-PBF samples. Upon completion of the AM process, the top surface of the as-built AISI316L samples were processed by laser polishing using a laser power of 70 W and a scan speed of 400 mm/s. For shot peening, the surface of the sample was shot peened for 20 min using a set-up similar to the one proposed by Naito et al. [48]. In summary, the surface mechanical treatment was a recirculating shot peening (hereafter called as shot peening) process utilizing balls (typically 1–6 mm diameter) made of stainless steel or ceramic. During the process, the surface of the samples is repeatedly impacted in random directions, and the shots are accelerated by a water jet with an injection pressure of 10 MPa. In this study, the

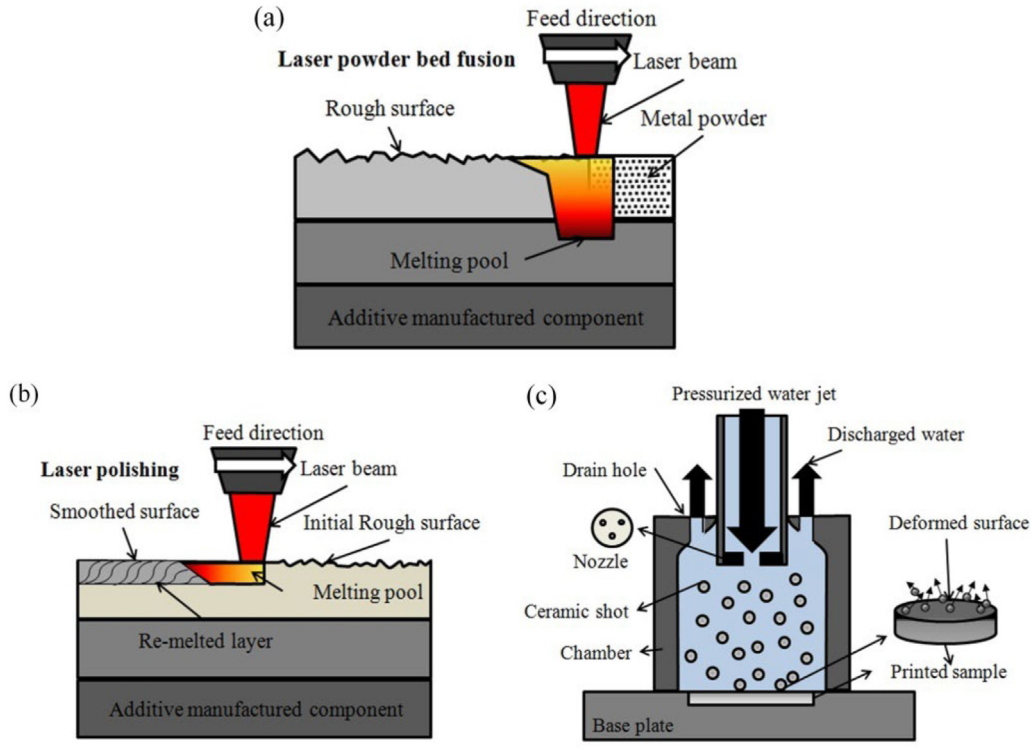

Fig. 2 – The schematic of (a) laser powder bed fusion process, (b) laser polishing, and (c) shot peening.

peening set-up was a home made system and 250 Zirconia ceramic shots with a smooth surface finish of 0.04 μm (*Ra*), 5 mm dimeter, and hardness of 1100 $HV_{0.1}$ were used for the surface treatment. The schematic of laser polishing and shot peening are shown in Fig. 2(b) and (c), respectively.

2.3. Material characterization

Non-contact 3D optical surface profiler (Zygo NewView 9000, United States) was used to investigate the effect of post-treatment on surface morphologies. Measurements were performed on a single field of view, with a Mirau 20× objective (field of view of 2 mm × 2 mm). The surface properties were analyzed according to the ISO25718 standard.

For microstructural examinations, the samples were first cross-sectioned, mounted in epoxy, ground down to 4000# grade SiC paper, and then polished with 1 μm diamond paste and 0.3 μm Al_2O_3 suspension. Finally, the samples were electropolished in ethanol and perchloric acid (8:2 vol/vol) solution at a direct current voltage of 20 V for 20 s. The microstructure of as-polished samples was studied in terms of the grain size evolution, grain boundary, and kernel average misorientation (KAM) using electron backscatter diffraction (EBSD) analysis and field-emission scanning electron microscopy (FE-SEM, Zeiss Sigma 500 VP). All the EBSD analyses were performed with an accelerating voltage of 25 kV and 100 nm scanning step size. EDAX OIM AnalysisTM software was used to analyze the raw data obtained from the EBSD analysis.

Surface residual stresses (RS) were estimated by the X-Ray Diffraction (XRD) technique and the standardized $\sin^2\psi$ method in the top surface of each sample, perpendicular to the build direction (BD), based on the relative position of the diffraction peak for hkl=(042) in the austenite lattice plane, which nominally appears at $2\theta = 144.62^\circ$ for AISI 316 L. The used X-ray elastic constants are $S_1 = -1.39 \times 10^{-6}$ 1/MPa and $\frac{1}{2}S_2 = 6.27 \times 10^{-6}$ 1/MPa with the assumed material constants E = 190 GPa and $\nu = 0.3$ [25,49].

Vickers microhardness measurements were performed on the top side of the samples using a diamond Vickers indenter under a load of 25 g that was applied for 15 s. A total of five measurements were carried out at different treated zones, and the average values were reported together with their standard deviations.

2.4. Electrochemical testing

The electrochemical experiments were performed on the as-printed, post-processed (laser polished or shot peened), and wrought AISI316L samples in a 0.9% NaCl solution at room temperature. Electrochemical measurements were controlled by a PARSTAT 2273 advanced electrochemical system with a conventional three-electrode cell system in which Ag/AgCl (Sat. KCl) acted as the reference electrode (RE) with the platinum foil and the metal surface acted as the counter electrode (CE) and the working electrode (WE), respectively. As-printed samples were used to examine the corrosion resistance affected by the original residual stress state and surface roughness. In addition, an as-printed sample's surface was ground to a 2000# grit finish before electrochemical tests to separate the effect of the surface roughness from that of residual stresses. Two series of laser polished and shot peened

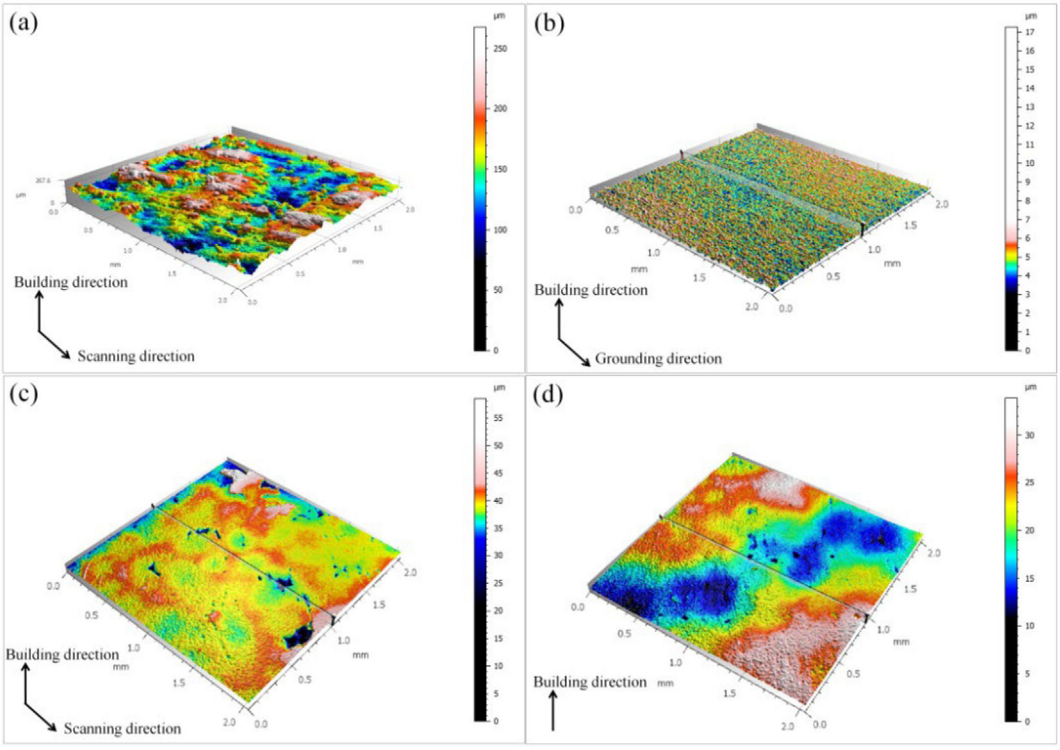

Fig. 3 – 3D surface topographies of the (a) as-printed, (b) ground, (c) laser polished and (d) shot peened samples.

samples were also analyzed with no grinding. Before the electrochemical tests, all the samples were thoroughly cleaned with ethanol and deionized water in an ultrasonic bath. The samples were then immersed for 45 min in the electrolyte prior to the electrochemical tests for stabilization, during which the open circuit potential (OCP) was measured. Cyclic potentiodynamic polarization scans were carried out from a −0.25 VAg/AgCl below the OCP to +1.1 VAg/AgCl at a scan rate of 1 mV/s. The scan direction reversed when current density values reached 100 μA/cm^2 thresholds, and the reversed scan continued until the samples were polarised down to −0.25 V below their respective OCP. Electrochemical impedance spectroscopy (EIS) was performed at open-circuit potential conditions and AC potential with an amplitude of 10 mV and 100 kHz to 10 mHz frequency range, with 15 points per decade. The equivalent circuits were generated using the electrochemical analyzer Z-View software. Mott-Schottky (MS) measurements were conducted to study the semiconducting type of the passive film. These measurements were carried out on the passive films at a frequency of 1 kHz using a 10 mV AC signal and a step potential of 10 mV by decreasing the applied potential in the cathodic direction from an initial potential 0.6 VAg/AgCl to a final potential of −1.0 VAg/AgCl. It should be noted that before the MS measurements, the samples were allowed to reach a stable corrosion potential. All the measurements have been repeated at least three times to ensure the reproducibility and consistency of the collected data.

3. Results and discussions

3.1. Surface roughness

3D topographies and various surface roughness parameters of as-printed and post-treated samples were obtained by 3D optical profilometry.

Based on the results reported in Fig. 3, the surface roughness of the as-printed sample was significantly higher than the rest of the samples. This discrepancy can be due to the unmelted or partially melted particles on the surfaces, along with the balling phenomenon, which could be optimized by adjusting the processing parameters. Compared to the as-printed sample, the top surfaces of the ground, laser polished, and shot peened samples were significantly smoother. The measured roughness of the post-treated samples exhibited a decreasing trend. The lowest surface roughness belonged to the ground sample with slight grinding marks, which was approximately twenty times lower than the as-printed one. After laser polishing, most surface defects, particularly partially melted powders, were remelted, creating a smoother surface than the as-printed one. In the case of shot peened sample, most of the surface peaks were removed or flattened by the impact of ceramic shots applied in various directions. Consequently, the surface became much smoother, with some residual valleys that are typical dimples induced by multiple impacts. Indeed, shot peening not only reduces the height of the peaks on the surface but also fills valleys producing a smoother surface eventually [50,51]. However, These features, along with collision effect of ceramic shots on the surface led to the formation of a slightly rougher surface in the shot peened sample compared to the laser polished one. The surface roughness values including average mean roughness (*Sa*) and maximum height of the roughness (*Sz*) of corresponding samples are compared in Fig. 4.

The average surface roughness parameter, *Sa*, for the as-printed sample was 14.11 ± 1.65 μm, which was reduced for the ground sample to 0.51 ± 0.25 μm, and for the laser polished and shot peened samples to 1.09 ± 0.46 μm and 1.66 ± 0.34 μm, respectively. The difference between the maximum peak and valley (*Sz*) was 240.19 ± 9.67 μm for the as-printed sample. This feature was measured to be 17.44 ± 3.31 μm, 22.25 ± 4.25 μm, and 58.52 ± 8.46 μm for the ground, laser polished, and shot peened samples, respectively. Therefore, it could be concluded from these results that post-processing is a very effective way to reduce the surface roughness of the AM parts. Among the two proposed methods in this study, laser polishing would be a better candidate to achieve lower surface roughness by choosing optimal parameters. However, shot peening-based methods, in addition to the surface smoothing, can also improve mechanical and corrosion properties, which is an important advantage over the laser polishing process [23,50–52].

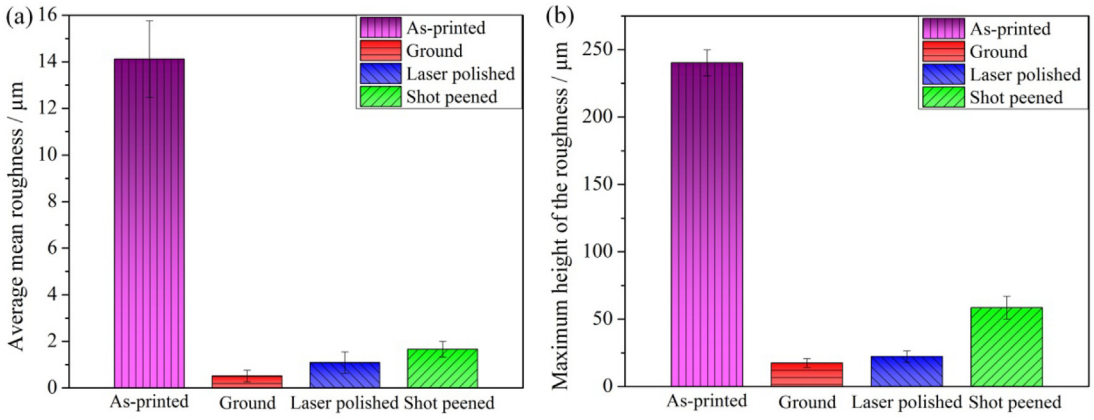

Fig. 4 – Surface roughness values of samples (a) average mean roughness (*Sa*) (b) maximum height of the roughness (*Sz*).

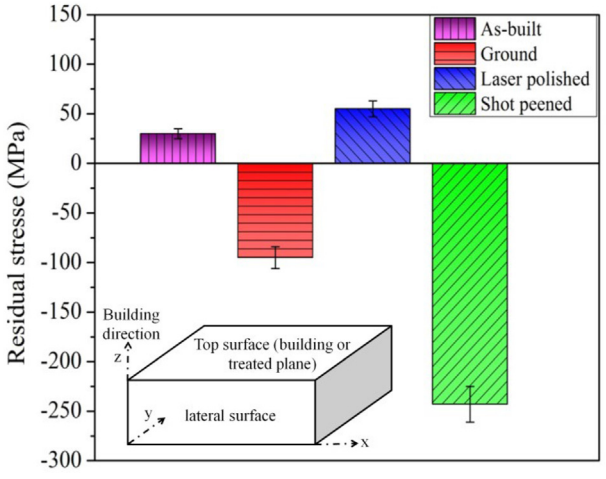

Fig. 5 – Average top surface residual stress for the samples.

3.2. *Residual stress*

The results of the surface residual stress measurements in the XY plane transverse to the BD by XRD analysis, are shown in Fig. 5. Tensile stresses were measured for the as-printed (30.6 ± 5.8 MPa) and laser polished (55.4 ± 8.1 MPa) samples. Simson et al. [25] reported that residual stresses on the top surface of L-PBF AISI316L samples were approximately 200 MPa. The authors reported that the magnitude of the surface residual stress highly depended on the L-PBF parameters. Tensile stress may have been generated during the heating and cooling cycles, and thermal stresses resulting from temperature gradients or solidification-induced shrinkage during fabrication for the as-printed and laser polished samples [25]. In contrast to the as-printed and laser polished samples, the residual stress on the top surfaces of the ground and shot peened samples was compressive, with the stress values being −95.7 ± 11.1 MPa and −243.7 ± 18.4 MPa, respectively. This finding is consistent with a previous work [50] emphasizing the effect of shot peening on the stress mode alteration of the AM sample's surface.

3.3. *Microstructural characterization*

EBSD analysis revealed the grain features and distribution of crystal defects for the as-printed sample and the post-processed ones. Fig. 6(a) shows the inverse pole figures (IPF) of the as-printed sample with columnar grains parallel to the BD on the XZ plane as a result of the high thermal gradient in the building direction. This high thermal gradient is usually linked to the high conductivity of the previously deposited layer, the small size of the melt pool created by the laser, and the high temperature at the melt pool hot spot [21]. Fig. 6(b) demonstrates that grains remained parallel to the BD when the remelting process was applied despite their enlarged size and altered crystallographic orientation. However, for the shot peened sample (Fig. 6(c)), it can be seen that the as-printed sample deformed severely due to the cold work induced by the multiple impacts while the grains were rotated and refined. Hence, it can be concluded that the grain morphology is strongly affected by the post-treatments. Fig. 6(d–f) displays the grain boundary distribution of different samples. As shown in Fig. 6(e) and (f), the microstructure of the shot peened sample contained more high angle grain boundaries (HAGBs: >15) than the as-printed sample. Indeed, a cellular sub-structure with low angle grain boundaries (LAGBs: 2–15) has been commonly observed in AISI316L samples produced via AM method. The formation of cellular substructure mainly originates from rapid solidification induced material deformation [23]. Upon laser polishing, the density of low angle grain boundaries was markedly reduced, a behavior which can be attributed to the annihilation of dislocations during the laser polishing process. It can be seen in Fig. 6(f) that LAGBs tend to form in the surface and subsurface of the shot peened sample. The grain boundaries observed inside large grains are mainly LAGBs, which tend to form near the surface. Hence the grains in the subsurface region are divided into small grains and more cellular sub-structure formed by LAGBs.

The fraction of LAGBs and HAGBs and grain boundary lengths (GBL) of the samples were statistically calculated

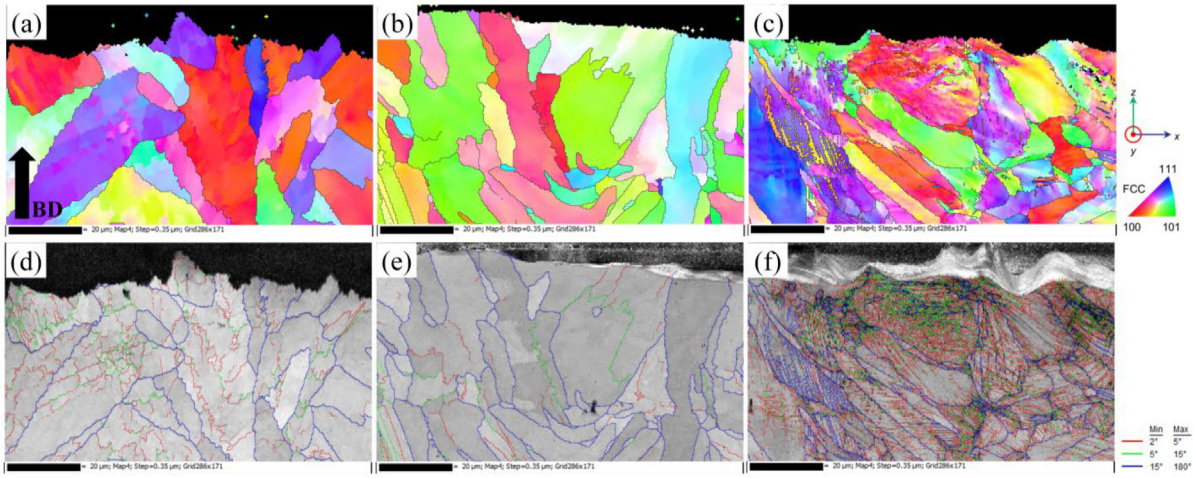

Fig. 6 – IPF images with grain boundaries: (a) as-printed, (b) laser polished, (c) shot peened, and Image quality with grain boundaries (d) as-printed, (e) laser polished, (f) shot peened.

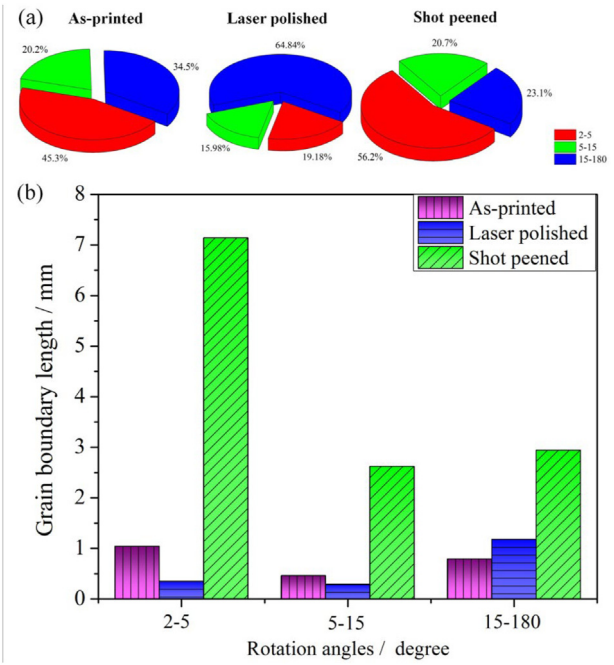

Fig. 7 – (a) Fraction of LAGBs and HAGBs and (b) the distribution of grain boundary length with rotation angle in the studied samples.

based on the EBSD results approximately 50 μm depth from the surface and reported in Fig. 7.

As shown in Fig. 7, it can be seen that the fraction of LAGBs and HAGBs on the cross-section of the shot peened sample, especially near the surface, is higher than the other two samples. Indeed, it should be noted that the HAGB fraction is greater than the LAGB fraction for the laser polished sample (as shown in Fig. 6), mainly due to the induced thermal effect and re-solidification of molten metal liquid during the remelting process. Fig. 7(a) and (b) show the length of different grain boundaries for the as-printed, laser polished and shot peened samples. As shown in Fig. 7(b), the total grain boundary length of the as-printed sample (2.29 mm) was roughly 1.2 times more than that of the laser polished one (1.82 mm). In comparison, the average length of low and high angle grain boundaries in the shot peened sample (12.70 mm) was about 7 times that of the laser polished sample.

Fig. 8 shows the KAM results of the as-printed AISI316L samples before and after post-treatment, which also depicts the dislocation distribution in the samples. According to the KAM maps, the shot peened sample (Fig. 8(c)) exhibited higher local KAM values, normally corresponding to a lattice strain or residual stress, compared to the as-printed one (Fig. 8(a)). This results would be attributed to the high density of dislocations generated during severe surface plastic deformation by the random impact of several shots repeatedly and concurrently applied on the surface, as reported for conventional shot peening applied to standard AISI316L [53].

This relatively higher KAM value near the surface and subsurface of the shot peened sample corresponds also to a greater level of lattice strain or residual stress. This finding is completely in line with the outcomes of the surface residual stress analysis, which are presented in Fig. 5. However, it can be noticed that the surface strain level of the as-printed sample decreased slightly after laser polishing (Fig. 8(b)) due to the thermal input during laser polishing, which led to stress relaxation and annihilation of dislocations.

According to the microhardness results shown in Fig. 9, the surface hardness of the as-printed, ground, laser polished and shot peened samples were 218 ± 21, 225 ± 19, 208 ± 11, and 284 ± 12 HV, respectively. After shot peening, the hardness of the sample was much higher than the as-printed and other post-processed samples. The grain boundaries and dislocation cells (Fig. 6(f)) can retard or block the migration of newly formed dislocations under external force, increasing the hardness and tensile strength [23,50].

Table 2 summarizes the investigated surface features, including roughness parameters, surface residual stress, microhardness, the fraction of LAGBs and HAGBs, and grain boundary lengths for the studied samples. The following section is dedicated to describe how these surface properties and microstructural changes influence the electrochemical behavior of the samples.

3.4. *Open circuit potentials and cyclic potentiodynamic polarization tests*

Representative open circuit potentials versus time for the as-printed sample and post-processed counterparts immersed in 0.9 wt% NaCl solution are plotted in Fig. 10(a). All the samples except for the as-printed one display similar electrochemical potential evolution tendency during immersion. In fact, the potential begins to rise slowly and stabilize during the test as a consequence of the reformation and thickening of the passive film on the electrode surface. However, The OCP trend of the as-printed condition changed erratically over the exposure time, whereas the ground sample was more stable; this observation indicates a dissolution dominant in the current

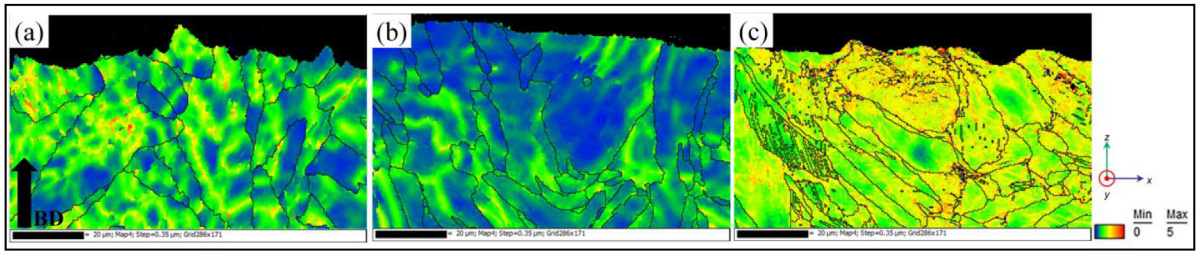

Fig. 8 – KAM results for the (a) as-printed, (b) laser polished, and (c) shot peened samples.

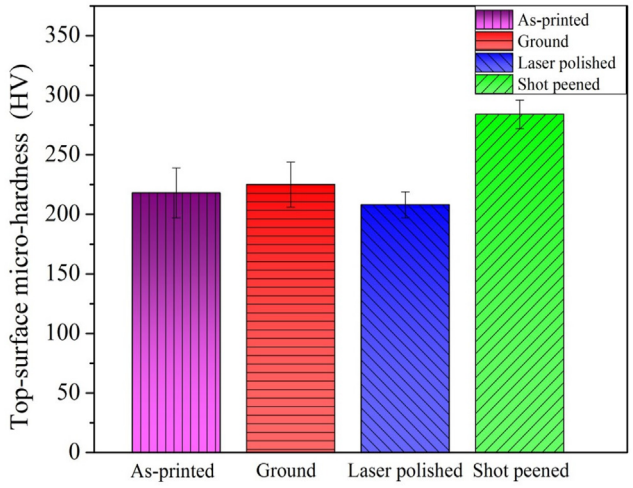

Fig. 9 – Average top surface microhardness of the studied samples.

condition as a consequence of high surface roughness for the as-printed sample (Fig. 3, Table 2).

Fig. 10(b) shows the cyclic potentiodynamic polarization curves of the as-printed and post-processed samples in a 0.9% NaCl solution. The polarization direction is indicated by black arrows in the plots. This method was used to determine the passive current density (I_{pass}), corrosion potential (E_{corr}), pitting potential (E_{pit}), and repassivation potential (E_{rep}) of the samples. Both I_{pass} and E_{corr} provide information on the interaction between the protective alloy surface and the corroding environment.

According to Fig. 10, the variation of the anodic polarization curve due to the surface post-treatment can be linked to the differences in surface properties, including roughness, crystal defects, and residual stress [21–23]. The electrochemical responses for the as-printed, post-processed, and wrought AISI316L samples in 0.9% NaCl solution are summarized in Table 3.

As seen in Table 3, the measured I_{pass} were 0.341 μA/cm^2, 1.162 μA/cm^2, 0.324 μA/cm^2 and 0.113 μA/cm^2 for the as-printed, ground, laser polished and shot peened AISI316L samples, respectively. The E_{corr} values varied from −0.245 $V_{Ag/AgCl}$ (for the wrought sample) to −0.122 $V_{Ag/AgCl}$ (for the shot peened sample). The apparent differences in corrosion behavior between the AM samples (as-printed and ground) and conventional wrought austenitic stainless steels can be primarily attributed to their different microstructural features [54]. The enlarged passivity of the as-printed and ground samples compared to the wrought sample could result from a more stable native oxide film [55]. Generally, AM austenitic stainless steels with minimal porosity exhibit better passivity

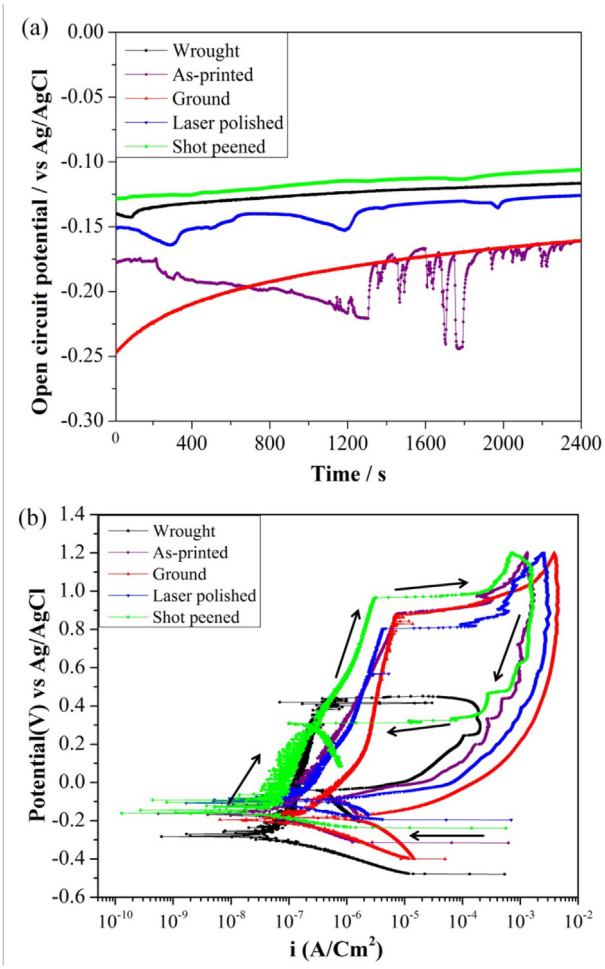

Fig. 10 – (a) Open circuit potential measurements, (b) Cyclic potentiodynamic polarization curves for all samples in 0.9% NaCl.

than their conventionally produced counterparts. Sander et al. [17] reported that in the case of an as-built AISI316L with a density over 99%, the resistance to pitting is generally increased compared to a conventionally made sample, thanks to the absence of MnS inclusions that reportedly act as the preferential sites for pit initiation. In conventionally-produced AISI316L samples, the dissolution of MnS inclusions is the most probable mechanism responsible for pit initiation, resulting in an aggressive local environment. Similar results were achieved in this work (Fig. 10).

However, surface roughness as an inherent characteristic of AM parts is one of the key parameters in determining their corrosion behavior since a rougher surface accelerates the electrochemical reactions between the surface and its immediate environment, leading to both general and localized

Table 2 – Surface modifications for as-printed and post processed samples.

	Sa, Sz (μm)	RS (MPa)	HV (25 g)	F_{LAGB}, F_{HAGB}	Total GBL (mm)
As-printed	14.11, 240.19	30	218	0.65, 0.34	2.29
Ground	0.51, 17.44	−95	225	–	–
Laser polished	1.09, 22.25	55	208	0.35,0.65	1.82
Shot peened	1.66, 58.52	−240	286	0.77,0.23	12.71

Table 3 – Summary of electrochemical parameters obtained in 0.9% NaCl environment.

Sample	I_{pass} ($\mu A/cm^2$)	E_{corr} ($V_{Ag/AgCl}$)	E_{pit} ($V_{Ag/AgCl}$)	E_{rep} ($V_{Ag/AgCl}$)	E_{pit}- E_{rep} ($V_{Ag/AgCl}$)
As-printed	0.341 ± 0.055	−0.168 ± 0.029	0.84 ± 0.17	−0.09 ± 0.02	0.93 ± 0.09
Ground	1.162 ± 0.078	−0.174 ± 0.012	0.89 ± 0.21	−0.18 ± 0.03	1.07 ± 0.12
Laser polished	0.324 ± 0.071	−0.192 ± 0.033	0.78 ± 0.16	−0.09 ± 0.07	0.87 ± 0.11
Shot peened	0.113 ± 0.023	−0.122 ± 0.019	0.96 ± 0.08	0.31 ± 0.06	0.65 ± 0.07
Wrought	0.122 ± 0.032	−0.245 ± 0.022	0.43 ± 0.11	−0.04 ± 0.02	0.47 ± 0.07

corrosion [23]. Comparing the as-printed and ground samples in Fig. 10 and Table 4, it can be noticed that decreasing the roughness of the surface lowers the electrochemical reactions, leading to a decrease in both general and localized corrosion. Moreover, during the polarization tests of the as-printed and ground samples, several current spikes were detected at the high anodic potential for the as-printed samples, indicating a metastable pit formation. In other words, there was a pre-existing passive layer on the sidewalls of partially melted particles and pores, but this protective layer was not stable enough and collapsed at higher anodic potentials causing fluctuations in the anodic branch of the polarization curve. Similar results were reported by other researchers working on the effect of surface roughness on the pitting resistance of AM AISI316L [33,34].

As shown in Fig. 10 and Table 3, the difference in I_{pass} value of the laser polished sample and as-printed one was minor. In addition, the corrosion potential (E_{corr}) was slightly negative after laser polishing. These findings imply that the formation of a higher tensile residual stress and decrease in surface crystal defects are the primary causes of the slight deterioration of the corrosion behavior in the laser polished samples. In other words, the higher tensile stress in laser polished samples may result in the creation of corrosion cells inside the structure, with stressed zones serving as anodic areas leading to a minor increase in corrosion rate [15,56].

The surface of the shot peened sample was observed to be more reactive than the other surfaces due to the higher density of crystal defects (Fig. 6). Therefore, according to Fig. 10, the polarization curves for the shot peened sample are noisy when cathodic reactions are still occurring, with the passive plateau exhibiting a wavy form, demonstrating that even in the passive state, certain sites are still reactive. In general, the compressive residual stresses and higher density of crystal defects on the surface of the as-printed sample are the most significant variables affecting corrosion resistance and passive film generation. The high density of crystal defects, such as grain boundaries and dislocations, provide ample nucleation sites for passive film formation and subsequently influence the passive film properties. To enhance the corrosion properties of the AM AISI316L parts, grain refinement is suggested by several researchers to improve the growth of the passive layer by decreasing the diffusion path length or, in other words increasing the diffusion rate for chromium atoms toward the surface to form a protective and homogeneous chromium oxide layer [37–40]. Overall, our findings are consistent with earlier research on the passive film characteristics of austenitic stainless steel showing the influence of grain size and residual stress levels [34,57–59].

The E_{pit} and E_{rep} mean values of the different samples as a function of roughness, residual stress, and grain boundary lengths of the individual samples are plotted in Fig. 11.

The E_{pit} values of all samples were found to be within the range 0.83–0.96 $V_{Ag/AgCl}$ (Table 3), which is about 400 mV higher than the E_{pit} of the wrought AISI316L sample. This behavior is related to the nature of the inclusions and their distribution within the microstructure, which commonly act as pit initiation sites on the metal surface and consequently decrease the susceptibility to pitting. Evidence of increased pitting corrosion values E_{pit} after post-treatment is provided by other researchers [21,30].

The formation of an unstable or thin passive film on a highly rough surface will eventually form steady-state pits and decrease the pitting potential [23,60,61]. It has also been demonstrated that the repassivation ability of the as-printed sample is relatively weaker than the ground samples, a behavior which is attributed to the surface roughness and partially melted particles on the surface (Fig. 11(a)). When the corrosive solution is confined in these regions, the chemistry of the solution alters, resulting in de-passivation and preventing the creation of a stable, uniform passive layer [21,22]. Also, defects such as partially melted particles, pores, and inclusions in the passive film (as-printed and wrought sample) trigger localized corrosion attacks through several mechanisms, like creating Cr-depleted regions or decreasing the repassivation ability of the alloy. On the other hand, the average E_{rep} for the shot peened sample was at least 0.32 $V_{Ag/AgCl}$, which was above the average E_{rep} recorded for other samples. E_{rep} was found to decrease with sample surface tensile residual stress (Fig. 11(b)). In other words, repassivation after stable pitting, as triggered by anodic polarization, was more favored in samples with compressive residual

Table 4 – Variations in the impedance parameters and passive film thickness of all samples in 0.9% NaCl.

Sample	Rs ($\Omega.cm^2$)	Rp ($k\Omega.cm^2$)	CPE ($\mu F.cm^{-2}$)	n	L (nm)
As-printed	328.2 ± 0.1	13.83 ± 0.17	7.85 ± 0.52	0.83 ± 0.05	1.8–2.1
Ground	312.9 ± 0.3	12.62 ± 0.22	1.12 ± 0.46	0.87 ± 0.04	2.4–2.7
Laser polished	304.7 ± 0.2	7.23 ± 0.18	6.81 ± 0.37	0.79 ± 0.07	2.2–2.5
Shot peened	328.9 ± 0.4	24.31 ± 1.56	6.75 ± 0.22	0.84 ± 0.11	3.6–3.9
Wourght	308.3 ± 0.7	5.04 ± 1.32	1.48 ± 0.72	0.82 ± 0.08	1.9–2.2

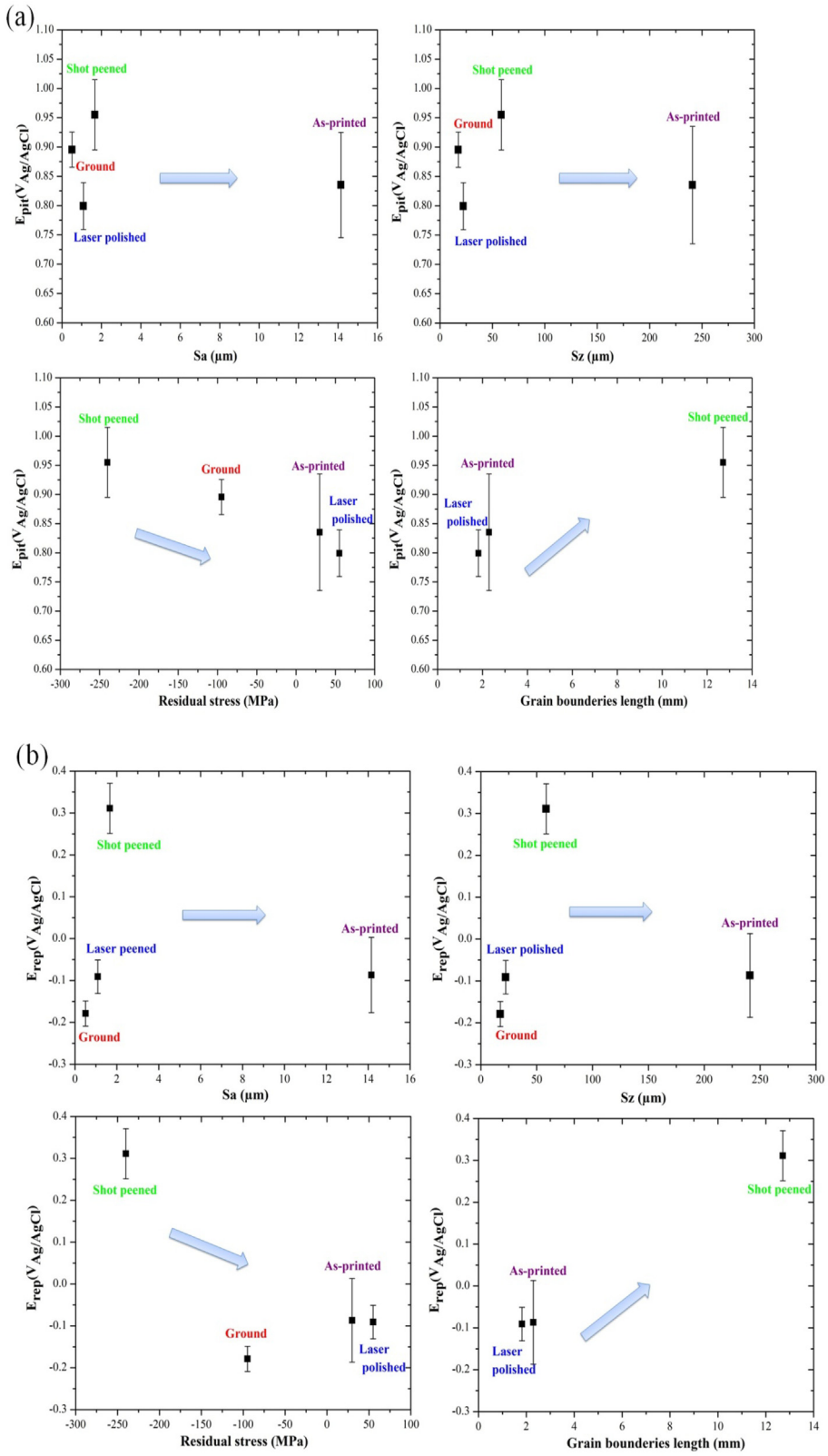

Fig. 11 – Relationships between (a) pitting potential and (b) repassivation potential as a function of surface roughness, residual stress, and grain boundaries length.

stress on the surface. All in all, it was observed that the shot peening treatment (Fig. 11(a and b)) induced more notable corrosion modifications compared to the other treatments. The significant improvements noticed for the shot peened samples can be due to the combined effect of a lower surface roughness with more regular surface morphology compared to the as-printed state along with compressive residual stress on the surface. In addition, formation of a high density of crystal defects on the surface may be considered as a positive factor influencing the corrosion behavior of the shot peened sample.

3.5. *Electrochemical impedance spectroscopy tests*

The EIS response of different samples in 0.9% NaCl solution was investigated at the open-circuit potential, and the results are shown as Nyquist and Bode-phase plots in Fig. 12. The experimental data are represented by symbol points, while the fitted data are represented by a straight line of the same color.

Based on the Nyquist plots (Fig. 12(a)), it can be pointed out that typical capacitive semi-loop shapes are similar for all samples, while the diameters are different. The imperfect semicircle diameter for the shot peened sample was higher than that of other series, reflecting better passivation behavior and formation of stable oxide film on the surface of the shot peened sample. However, the roughness (as-printed vs. ground) and residual stress (as-printed vs. laser polished) had no significant effect on the stability of the passive film. Therefore, similar to the cyclic potentiodynamic polarization curves, the differences between the as-printed and ground parts are rather low. More specifically, as seen in Fig. 12 (b), the Bode-phase curves show one time constant (only one maximum phase angle at the middle frequency range). It seems that at or near OCP, the mechanism of corrosion reaction for all samples was the same and mainly controlled by the charge transfer phenomena through the protective layer. Also, the constant phase nature of the impedance at low frequencies is a consequence of defect transport within the oxide film, mainly due to the migration of metal ions and vacancies under the influence of the electric field. Hence, the phase angle values remained very close to −75°, revealing the formation and growth of a passive film for all samples. Moreover, to simulate the measured impedance data, a simple circuit (Fig. 10(c)) comprising of solution resistance (Rs), polarization resistance (Rp), and constant phase element (CPE) was used for fitting the EIS data (Fig. 10(a)). It can be seen that the CPE is parallelly connected to an oxide film resistance (Rp) and serially to the previous two components with a solution resistance (Rs). The electrical impedance of CPE can be calculated by Eq. (1) [34]:

$$Z_{CPE} = \frac{1}{Q(\omega j)^{n}} \quad (1)$$

where Q, ω, n, and j are constant, angular frequency, capacitor coefficient behavior and the imaginary factor, respectively. The factor n is the dispersion index, and the value of n indicates the deviation from the pure capacitor where n = 1. The variation of the impedance parameters obtained from fitting the EIS data of the wrought, as-printed, and post-processed samples in a 0.9% NaCl solution is illustrated in Table 4.

According to the EIS results, the shot peened sample exhibited better barrier properties (higher polarization resistance). This enhanced passivity for the shot peened sample can be attributed to residual stress and crystal defects due to the mechanical treatment. In other words, it is suggested that the construction and growth of the passive film may be modified by increased lattice defects and compressive stress levels in the substrate. Indeed, the residual stress changes the inter-atomic distance, and a narrower inter-atomic distance obtained by compressive residual stress increases the probability of the presence of Cr atoms at the metal/environment interface AISI316L sample. This phenomenon leading to prevent the migration of point defects across the passive film and the formation of passive film enriched in Cr-oxides [57]. However, according to the results obtained for the as-printed sample compared to the laser polished or ground samples, it seems that the residual stress at or near OCP has no significant effect on the polarization resistance and stability of the passive film. Similar results were also reported by Cruz et al. [34], where L-PBF AISI316L samples with different residual stress

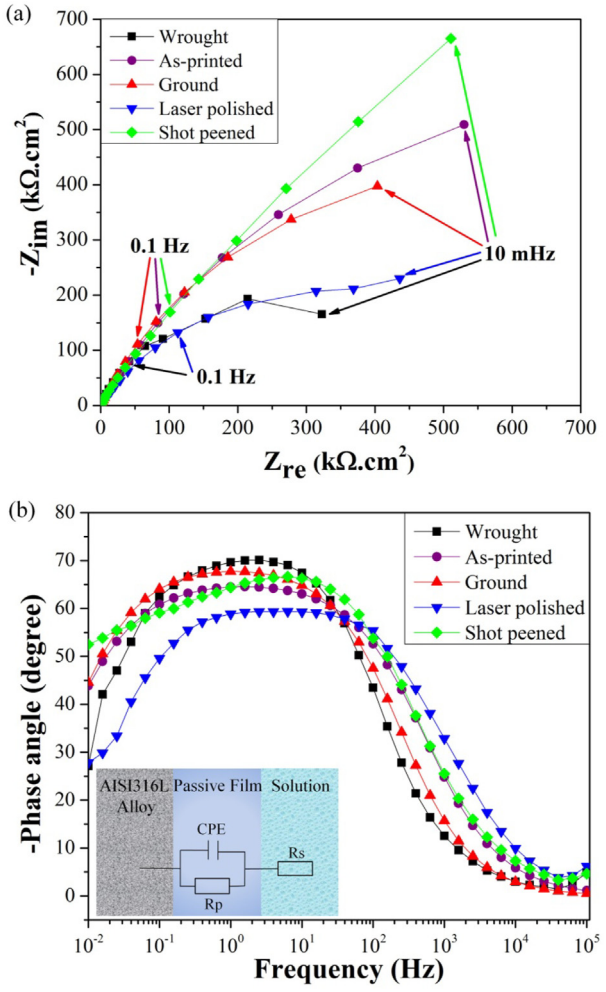

Fig. 12 – EIS plots for the as-printed and post-processed AISI316L samples: (a) Nyquist plots, (b) Bode plots (Inset shows the equivalent circuit used to fit the data).

levels had similar charge transfer resistances as the as-built sample. On the other hand, an increase in the density of crystal defects such as dislocations and grain boundaries (Fig. 8(c)) promotes the diffusion of passivating elements (like Cr) towards the surface, enabling the rapid formation of a homogeneous, thicker, Cr-enriched, and compact passive film. To elaborate this behavior, the variation of the passive film thickness (L_{ss}) of the studied samples were calculated using the following Eq. (2) [62]:

$$\mathrm{Lss} = \frac{\varepsilon\varepsilon_0 \mathrm{A}}{C_f} \tag{2}$$

where ε_0 is the vacuum permittivity (8.854×10^{-14} Fcm^{-1}), ε is the dielectric constant for the passive film (15.6 for stainless steel [34,63,64]), A is the effective area of the electrode, and C_f is the total capacitance of the passive film measured from the EIS results, after the formation of the oxide film [65]. This equation demonstrates that any change in the total capacitance of the passive film is indicative of variation in the passive film thickness. In other words, an inverse relationship between capacitance and the thickness of the passive film was noticed in this investigation, whereby grain refinement was more effective than the surface roughness and residual stress. The total capacitance of the passive film is obtained from Eq. (3) [66]:

$$C = -\frac{1}{2\pi f Z''} \tag{3}$$

where Z″ is the imaginary component of the impedance and f is the frequency. The 1000 Hz is used in this study. The calculated values for L are shown in Table 4, which are in agreement with the previous studies [55,67].

Therefore, surface mechanical post-treatment, simultaneously inducing crystal defects, compressive residual stress, and work hardening, facilitate the formation of a thicker passive film that seems to be the most pertinent factor behind the corrosion resistant improvement against passive layer rupture.

3.6. Mott-Schottky analysis

Generally, oxide films with perfect crystal structures can be considered as insulators. However, the presence of point defects in the passive films, such as oxygen vacancies and cation interstitials, can make them behave as extrinsic semiconductors when exposed to an aqueous solution. Indeed, the physico-chemical properties of the passive films are dominated by the point defects motion and distribution, which are responsible for the passive film's steady state. Mott–Schottky analysis has been employed to determine the semiconductor type and dopant density of the passive film [64,65,68].

According to the Mott–Schottky theory, the space charge capacitances (CSC) of n-type and p-type semiconductors can be calculated by Eqs. (4) and (5), respectively:

$$\frac{1}{C_{SC}{}^2} = \frac{2}{e\varepsilon\varepsilon 0 N_D}\left(E - E_{fb} - \frac{k_B T}{e}\right) \tag{4}$$

$$\frac{1}{C_{SC}{}^2} = -\frac{2}{e\varepsilon\varepsilon 0 N_A}\left(E - E_{fb} - \frac{k_B T}{e}\right) \tag{5}$$

where e is the electron charge (1.6×10^{-19} C), N_D and N_A are the donor and acceptor density (cm^{-3}), respectively. The variables E, E_{fb}, k_B, T are the applied potential (in $V_{Ag/AgCl}$), flat band potential (in $V_{Ag/AgCl}$), and the Boltzmann's constant and absolute temperature, respectively. Fig. 13 represents the electrode capacitance versus applied potential plots for a passive film formed on the as-printed and post-processed samples in a 0.9% NaCl solution. All plots reveal two linear parts indicating the Mott–Schottky-type (n-type and p-type semiconductor) behavior. As depicted in Fig. 13, the passive film capacitance is lower for the shot peened sample compared to the ground and as-printed ones, all having lower capacitance with respect to the laser polished sample. This decrement in the passive film capacitance suggests lower dissolution and an increase in the passivity of the shot peened samples compared to the other series.

As shown in Fig. 13, positive slopes within the potential range −400 to +100 $mV_{Ag/AgCl}$ indicate n-type semiconductor behavior of passive film formed on all the L-PBF AISI316L samples [34,65,69,70]. From the linear part of the plot, the donor density of the passive layer can be estimated using Eq. (6):

$$\mathrm{N_d} = \frac{2}{\varepsilon\varepsilon_0 e a} \tag{6}$$

where a is the slope in n-type region. The donor density calculated with this method indicates the density close to the passive film/alloy interface, which is directly related to the concentration of point defects in the passive film, such as oxygen vacancies or metal interstitials in an n-type semiconducting oxide layer [65,71]. The donor density values for the passive films formed on all the samples are plotted as a function of the surface roughness, residual stress and grain boundaries length in Fig. 14. For all the samples, the density is about 10^{20} cm^{-3}, which is in excellent agreement with the data reported in the literature [67,72,73].

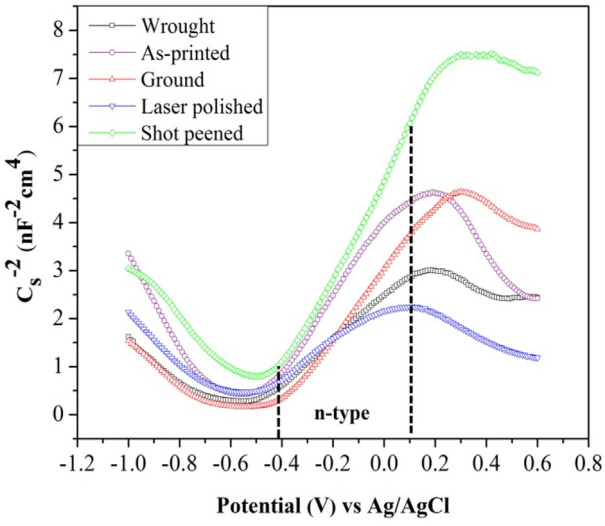

Fig. 13 – Mott-Schottky curves at frequency 1 kHz measured in the cathodic direction for all samples in 0.9% NaCl.

According to Fig. 14, almost similar results were obtained for the as-printed and ground samples. However, the donor density of the passive film formed on the shot peened sample was less than that of the as-printed sample, which reflected better passivation behavior of the shot peened sample. In other words, the number of point defects was decreased in the passive film formed on the shot peened sample, while the as-printed sample exhibited a highly defective passive film. On the other hand, for the laser polished sample, a lower roughness and a higher tensile residual stress led to a slight decrease in the donor density and point defect concentration within the passive film, as compared to the as-printed sample. Generally, a higher donor density value indicates a higher conductivity and lower oxide film quality with n-type semiconductive properties [69]. Moreover, based on the point defect model (PDM) [65,71,74], the above results show that the donor density and electrostatic field within the passive film are affected by surface roughness, crystal defect density, and the state of the residual stress on the surface. Overall, it was noticed that by increasing the crystal defects such as grain boundaries and dislocations, known as rapid path diffusion of elements, and inducing compressive residual stress, the kinetics of the interfacial reactions at the metal/film (generation of oxygen vacancies), film/solution interfaces (annihilation of oxygen vacancies), and also within the passive film became faster. This phenomenon led to the formation of a denser passive film on the shot peened sample compared to the other samples, demonstrating an improved electrochemical response. Therefore, it should be noted that the high density crystal defects generated a passive film containing richer Cr by promoting the Cr diffusion towards the surface, which may strengthen the passive film [23,64].

Considering the obtained results, it can be concluded from Fig. 15 that the lower pitting potential of the as-printed sample, compared to the ground and shot peened ones (Table 3), was mainly attributed to the increased donor density and point defect concentration of the passive film. Overall, crystal defects and compressive residual stresses decrease the donor density within the passive film, eventually affecting the pitting nucleation and metastable pitting process and reducing the transition probability from the metastable pitting to the stable pitting. Therefore, the lower the defect densities, the higher the pitting corrosion resistance.

Schematic representations of the effect of different post-treatments on sample's behavior after immersion in a corrosion environment at room temperature are shown in Fig. 16. Various parameters such as roughness, crystal defects, work hardened zone, residual stress, and corrosion characteristics discussed in the previous sections are detailed on these diagrams.

The surface of the as-printed sample is rough and under tensile residual stress in Fig. 16(a), but the surfaces of ground

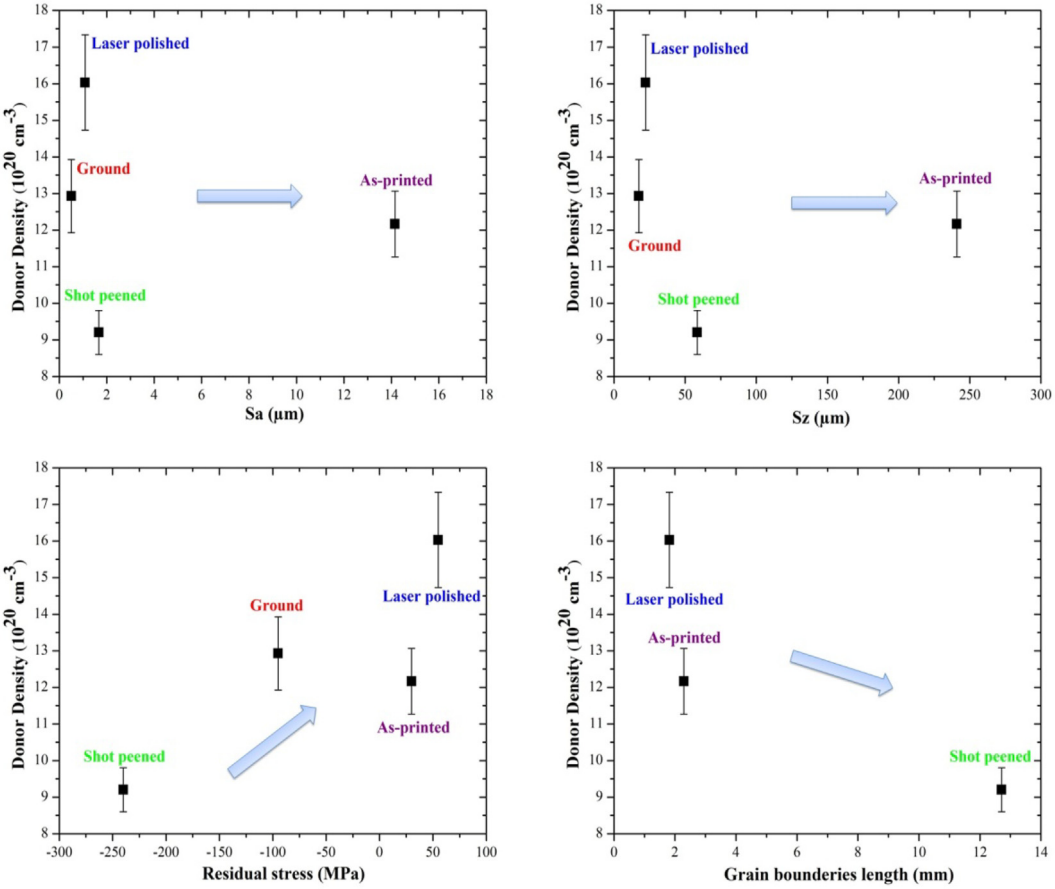

Fig. 14 – Relationship between donor density as a function of surface roughness, residual stress and grain boundaries length.

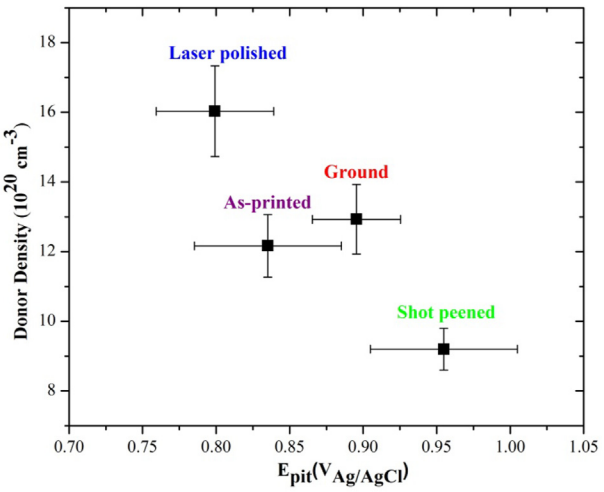

Fig. 15 – Relationship between donor density and pitting potential for the as-printed and post treated samples.

and shot peened samples (Fig. 16(b) and (d)) are smoother and under compressive residual stress. Moreover, the surface of the laser polished sample, shown in Fig. 16(c), featured low surface roughness and high tensile stress, unlike the other samples. However, from the crystal defects point of view, the shot peened surface exhibited a high density of crystal defects due to the plastic deformation and work hardening effect (Fig. 7 and Table 2).

As a passive film grows on all the surfaces, each previous factor can affect all the elementary processes associated with corrosion, i.e., charge transfer, film defects, film growth, and film stability. Indeed, these modifications have an impact on the current densities, the existence of the passive state and the occurrence of pitting [67,69,71,75]. It is reported that the stress level and lattice microstrain (that are directly related to KAM (Fig. 8) and microhardness (Fig. 9) values) are inversely proportional to interatomic distances at the metal surface [23,57,76]. Hence, it would be reasonable to assume that samples with higher KAM values (Fig. 8) have a higher atomic density at the surface. Moreover, higher compressive residual stress that is directly relevant to higher microstrain could reduce the required activation energy for the dissolution of atoms at metal/solution interfaces [40,76]. In the meantime, increasing crystal defect density (i.e., grain boundaries and dislocations) induced by plastic deformation promotes atomic diffusion in the upper-most subsurface zones and increases nucleation sites for the growth of the passive film. Hence, more available metal ions and nucleation sites facilitate the creation of a denser passive layer, including less point defect concentrations and consequently affect the corrosion prosperities [40,77,78].

Therefore, in terms of the metallurgical state of the surface, after the samples are immersed in corrosion media, as-printed sample is characterized by a very high donor density and a thin film (Fig. 13 and Table 3), which is grown on a rough surface with tensile residual stress. The edge effect probably

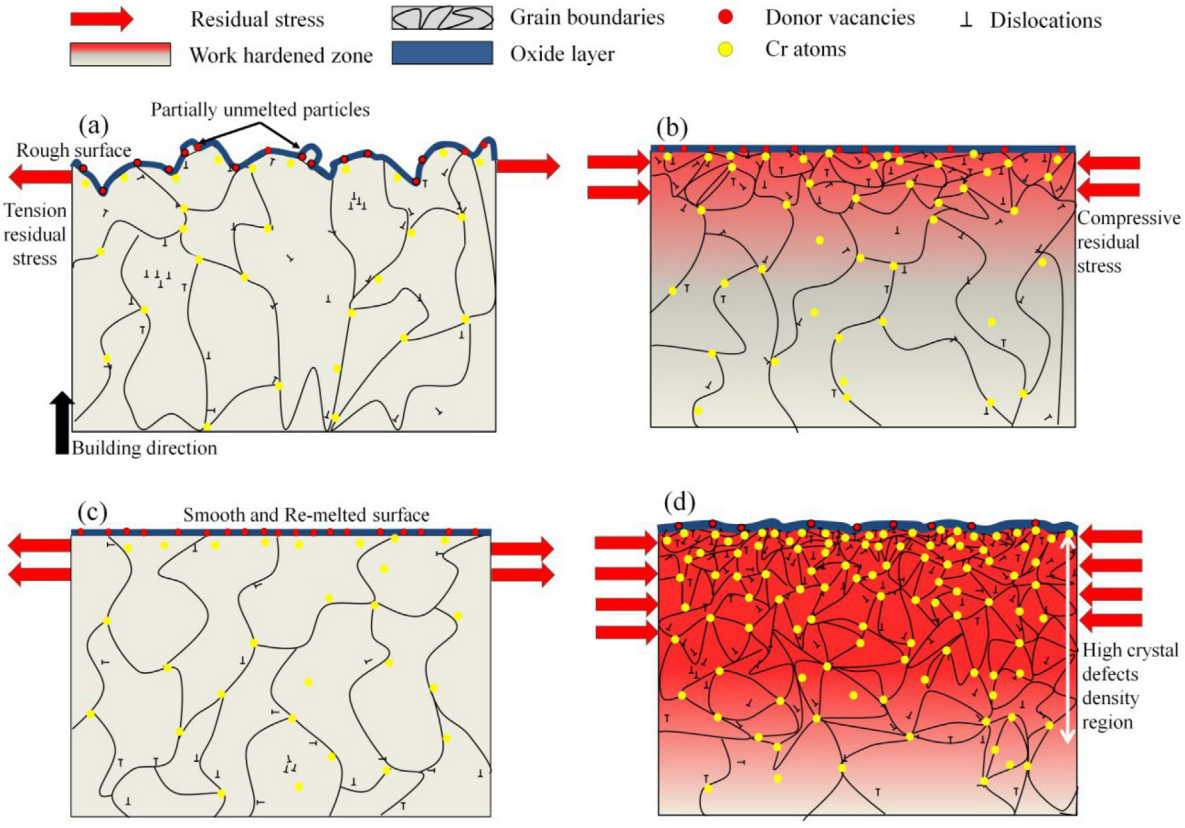

Fig. 16 – Schematics of surface modifications and passive film formation on the surface of (a) as-printed, (b) ground, (c) laser polished, and (d) shot peened samples.

promotes the injection of point defects thanks to the rough surface created in the as-printed sample [79]. However, the passive film formed on the ground surface is thicker, with a lower doping density and almost no roughness, having compressive residual stress. On the other hand, the passive film thickness formed on the laser polished surface is higher than a disordered surface (as-printed) because the surface becomes smooth, and the passive layer tends to become more stable. Finally, the passive film formed on the shot peened surface is the thickest, with the lowest doping density among all other samples. The lower surface roughness of shot peened series, the compressive residual streeses and the higher density of crystal defects such as grain boundaries and dislocations caused by surface plastic deformation that enhance the reactivity of the surface, play essential roles in the passive film properties of metallic AM samples.

4. Conclusions

The present study investigated the corrosion behavior of AISI316L samples produced via laser powder bed fusion AM method before and after different surface post-treatments including grinding, laser polishing and shot peening; the results were compared with those of a wrought sample. The main conclusions can be summarized as follow.

1 Based on the results obtained from EBSD analysis, grain boundary lengths and dislocation density on the surface of the shot peened samples were remarkably higher than the other series. This promoted surface hardness and induced compressive residual stresses on the surface. However, for the laser polished sample, the density of low angle grain boundaries was markedly reduced as a consequence of thermal input during the remelting process, where the dislocations were annihilated.
2 Electrochemical examinations demonstrated an increased pitting potential (mainly after shot peening) due to the high lattice defects density and large compressive stresses, which play an important role in reducing pit formation. The E_{pit} values were found to increase while $E_{pit}-E_{rep}$ values were also decreased by the increase of crystal defect density and compressive residual stress.
3 According to the EIS results, there was no significant difference in the electrochemical impedance and stability of the passive films formed on the as-printed, ground and laser polished samples. However, significant differences were observed in the polarization resistance (R_p) of the oxide layer of the shot peened samples, suggesting that the crystal defects of passive alloys could affect the passivation process by changing the element's diffusion rate. Moreover, the film grown on the shot peened sample was slightly thicker than the other samples.
4 Based on the point defect model and Mott-Schottky analysis, it is hypothesized that induced compressive residual stress and increased crystal defect density on the sample surface induced by shot peening could increase the resistance of the passive layer against defect transport and pit initiation. The modifications of the surface properties with the peening-based mechanical treatment lowered the donor density and point defect concentration in the passive film.

Declaration of competing interest

The authors declare that they have no known competing financial interests or personal relationships that could have appeared to influence the work reported in this paper.

REFERENCES

[1] Herzog D, Seyda V, Wycisk E, Emmelmann C. Additive manufacturing of metals. Acta Mater 2016. https://doi.org/10.1016/j.actamat.2016.07.019.
[2] Saboori A, Aversa A, Marchese G, Biamino S, Lombardi M, Fino P. Microstructure and mechanical properties of AISI 316L produced by directed energy deposition-based additive manufacturing: a review. Appl Sci 2020;10. https://doi.org/10.3390/app10093310.
[3] Yap CY, Chua CK, Dong ZL, Liu ZH, Zhang DQ, Loh LE, Sing SL. Review of selective laser melting: materials and applications. Appl Phys Rev 2015;2:041101. https://doi.org/10.1063/1.4935926.
[4] Sames WJ, List FA, Pannala S, Dehoff RR, Babu SS. The metallurgy and processing science of metal additive manufacturing. Int Mater Rev 2016;61:315–60. https://doi.org/10.1080/09506608.2015.1116649.
[5] Galati M, Defanti S, Saboori A, Rizza G, Tognoli E, Vincenzi N, Gatto A, Iuliano L. An investigation on the processing conditions of Ti-6Al-2Sn-4Zr-2Mo by electron beam powder bed fusion: microstructure, defect distribution, mechanical properties and dimensional accuracy. Addit Manuf 2022;50:102564. https://doi.org/10.1016/j.addma.2021.102564.
[6] Aristizabal M, Jamshidi P, Saboori A, Cox SC, Attallah MM. Laser powder bed fusion of a Zr-alloy: tensile properties and biocompatibility. Mater Lett 2020;259:126897. https://doi.org/10.1016/j.matlet.2019.126897.
[7] Mosallanejad MH, Niroumand B, Aversa A, Manfredi D, Saboori A. Laser powder bed fusion in-situ alloying of Ti-5% Cu alloy: process-structure relationships. J Alloys Compd 2021;857:157558. https://doi.org/10.1016/j.jallcom.2020.157558.
[8] Nedjad SH, Yildiz M, Saboori A. Solidification behaviour of austenitic stainless steels during welding and directed energy deposition. Sci Technol Weld Join 2022:1–17. https://doi.org/10.1080/13621718.2022.2115664. 0.
[9] Saboori A, Gallo D, Biamino S, Fino P, Lombardi M. An overview of additive manufacturing of titanium components by directed energy deposition: microstructure and mechanical properties. Appl Sci 2017;7. https://doi.org/10.3390/app7090883.
[10] Dadkhah M, Mosallanejad MH, Iuliano L, Saboori A. A comprehensive overview on the latest progress in the additive manufacturing of metal matrix composites: potential, challenges, and feasible solutions. Acta Metall Sin 2021;34:1173–200. https://doi.org/10.1007/s40195-021-01249-7.
[11] Cherry JA, Davies HM, Mehmood S, Lavery NP, Brown SGR, Sienz J. Investigation into the effect of process parameters on microstructural and physical properties of 316L stainless steel parts by selective laser melting. Int J Adv Manuf Technol 2015;76:869–79. https://doi.org/10.1007/s00170-014-6297-2.

[12] Marchese G, Parizia S, Saboori A, Manfredi D, Lombardi M, Fino P, Ugues D, Biamino S. The influence of the process parameters on the densification and microstructure development of laser powder bed fused inconel 939. Metals 2020;10. https://doi.org/10.3390/met10070882.
[13] Sohrabpoor H, Salarvand V, Lupoi R, Chu Q, Li W, Aldwell B, Stanley W, O'Halloran S, Raghavendra R, Choi CH, Brabazon D. Microstructural and mechanical evaluation of post-processed SS 316L manufactured by laser-based powder bed fusion. J Mater Res Technol 2021;12:210–20. https://doi.org/10.1016/J.JMRT.2021.02.090.
[14] Chao Q, Thomas S, Birbilis N, Cizek P, Hodgson PD, Fabijanic D. The effect of post-processing heat treatment on the microstructure, residual stress and mechanical properties of selective laser melted 316L stainless steel. Mater Sci Eng 2021;821:141611. https://doi.org/10.1016/j.msea.2021.141611.
[15] Chen L, Richter B, Zhang X, Ren X, Pfefferkorn FE. Modification of surface characteristics and electrochemical corrosion behavior of laser powder bed fused stainless-steel 316L after laser polishing. Addit Manuf 2020;32:101013. https://doi.org/10.1016/j.addma.2019.101013.
[16] Saboori A, Toushekhah M, Aversa A, Lai M, Lombardi M, Biamino S, Fino P. Critical features in the microstructural analysis of AISI 316L produced by metal additive manufacturing. Metallogr Microstruct Anal 2020;9:92–6. https://doi.org/10.1007/s13632-019-00604-6.
[17] Sander G, Thomas S, Cruz V, Jurg M, Birbilis N, Gao X, Brameld M, Hutchinson CR. On the corrosion and metastable pitting characteristics of 316L stainless steel produced by selective laser melting. J Electrochem Soc 2017;164:C250–7. https://doi.org/10.1149/2.0551706jes.
[18] Sander G, Babu AP, Gao X, Jiang D, Birbilis N. On the effect of build orientation and residual stress on the corrosion of 316L stainless steel prepared by selective laser melting. Corrosion Sci 2021;179. https://doi.org/10.1016/j.corsci.2020.109149.
[19] Lodhi MJK, Deen KM, Greenlee-Wacker MC, Haider W. Additively manufactured 316L stainless steel with improved corrosion resistance and biological response for biomedical applications. Addit Manuf 2019;27:8–19. https://doi.org/10.1016/j.addma.2019.02.005.
[20] Wang D, Liu Y, Yang Y, Xiao D. Theoretical and experimental study on surface roughness of 316L stainless steel metal parts obtained through selective laser melting. Rapid Prototyp J 2016;22:706–16. https://doi.org/10.1108/RPJ-06-2015-0078.
[21] Laleh M, Hughes AE, Xu W, Gibson I, Tan MY, Laleh M, Hughes AE, Xu W, Gibson I, Tan MY. A critical review of corrosion characteristics of additively manufactured stainless steels. Int Mater Rev 2020:1–37. https://doi.org/10.1080/09506608.2020.1855381. 0.
[22] Scully JR, Birbilis N. Corrosion of additively manufactured alloys: a review. 9312. 2018. p. 1318–50.
[23] Ettefagh AH, Guo S. Journal Prproo. Addit Manuf 2020:101689. https://doi.org/10.1016/j.addma.2020.101689.
[24] Melia MA, Duran JG, Koepke JR, Saiz DJ, Jared BH, Schindelholz EJ. How build angle and post-processing impact roughness and corrosion of additively manufactured 316L stainless steel. Npj Mater Degrad 2020;4. https://doi.org/10.1038/s41529-020-00126-5.
[25] Simson T, Emmel A, Dwars A, Böhm J. Residual stress measurements on AISI 316L samples manufactured by selective laser melting. Addit Manuf 2017;17:183–9. https://doi.org/10.1016/j.addma.2017.07.007.
[26] Barros R, Silva FJG, Gouveia RM, Saboori A, Marchese G, Biamino S, Salmi A, Atzeni E. Stress analysis before and after heat treatment. Metals 2019;9:1290. https://www.mdpi.com/2075-4701/9/12/1290.
[27] Chao Q, Cruz V, Thomas S, Birbilis N, Collins P, Taylor A, Hodgson PD, Fabijanic D. On the enhanced corrosion resistance of a selective laser melted austenitic stainless steel. Scr Mater 2017;141:94–8. https://doi.org/10.1016/j.scriptamat.2017.07.037.
[28] Man C, Duan Z, Cui Z, Dong C, Kong D, Liu T, Chen S, Wang X. The effect of sub-grain structure on intergranular corrosion of 316L stainless steel fabricated via selective laser melting. Mater Lett 2019;243:157–60. https://doi.org/10.1016/j.matlet.2019.02.047.
[29] Martin AA, Calta NP, Khairallah SA, Wang J, Depond PJ, Fong AY, Thampy V, Guss GM, Kiss AM, Stone KH, Tassone CJ, Nelson Weker J, Toney MF, van Buuren T, Matthews MJ. Dynamics of pore formation during laser powder bed fusion additive manufacturing. Nat Commun 2019;10:1987. https://doi.org/10.1038/s41467-019-10009-2.
[30] Zhang B, Li Y, Bai Q. Defect Formation mechanisms in selective laser melting: a review. Chin J Mech Eng 2017;30:515–27. https://doi.org/10.1007/s10033-017-0121-5.
[31] Khairallah SA, Anderson AT, Rubenchik A, King WE. Laser powder-bed fusion additive manufacturing: physics of complex melt flow and formation mechanisms of pores, spatter, and denudation zones. Acta Mater 2016;108:36–45. https://doi.org/10.1016/j.actamat.2016.02.014.
[32] Zou S, Xiao H, Ye F, Li Z, Tang W, Zhu F, Chen C, Zhu C. Numerical analysis of the effect of the scan strategy on the residual stress in the multi-laser selective laser melting. Results Phys 2020;16:103005. https://doi.org/10.1016/j.rinp.2020.103005.
[33] Chen S, Gao H, Zhang Y, Wu Q, Gao Z, Zhou X. Review on residual stresses in metal additive manufacturing: formation mechanisms, parameter dependencies, prediction and control approaches. J Mater Res Technol 2022;17:2950–74. https://doi.org/10.1016/j.jmrt.2022.02.054.
[34] Cruz V, Chao Q, Birbilis N, Fabijanic D, Hodgson PD, Thomas S. Electrochemical studies on the e ff ect of residual stress on the corrosion of 316L manufactured by selective laser melting. Corrosion Sci 2020;164:108314. https://doi.org/10.1016/j.corsci.2019.108314.
[35] Sun Y, Bailey R, Moroz A. Surface finish and properties enhancement of selective laser melted 316L stainless steel by surface mechanical attrition treatment. Surf Coating Technol 2019;378:124993. https://doi.org/10.1016/j.surfcoat.2019.124993.
[36] Shahryari A, Kamal W, Omanovic S. The effect of surface roughness on the efficiency of the cyclic potentiodynamic passivation (CPP) method in the improvement of general and pitting corrosion resistance of 316LVM stainless steel. Mater Lett 2008;62:3906–9. https://doi.org/10.1016/j.matlet.2008.05.032.
[37] Zhao C, Bai Y, Zhang Y, Wang X, Xue JM, Wang H. Influence of scanning strategy and building direction on microstructure and corrosion behaviour of selective laser melted 316L stainless steel. Mater Des 2021;209. https://doi.org/10.1016/j.matdes.2021.109999.
[38] Chai R, Zhang Y, Zhong B, Zhang C. Effect of scan speed on grain and microstructural morphology for laser additive manufacturing of 304 stainless steel. Rev Adv Mater Sci 2021;60:744–60. https://doi.org/10.1515/rams-2021-0068.
[39] Ettefagh AH, Guo S. Electrochemical behavior of AISI316L stainless steel parts produced by laser- based powder bed fusion process and the e ff ect of post annealing process. Addit Manuf 2018;22:153–6. https://doi.org/10.1016/j.addma.2018.05.014.
[40] Morshed-Behbahani K, Zakerin N. A review on the role of surface nanocrystallization in corrosion of stainless steel. J Mater Res Technol 2022;19:1120–47. https://doi.org/10.1016/j.jmrt.2022.05.094.

[41] Muley SV, Vidvans AN, Chaudhari GP, Udainiya S. An assessment of ultra fine grained 316L stainless steel for implant applications. Acta Biomater 2016;30:408–19. https://doi.org/10.1016/j.actbio.2015.10.043.
[42] Basha SM, Bhuyan M, Basha MM, Venkaiah N, Sankar MR. Laser polishing of 3D printed metallic components: a review on surface integrity. Elsevier Ltd Mater Today Proc 2019:2047–54. https://doi.org/10.1016/j.matpr.2020.02.443.
[43] Ye C, Zhang C, Zhao J, Dong Y. Effects of post-processing on the surface finish, porosity, residual stresses, and fatigue performance of additive manufactured metals: a review. J Mater Eng Perform 2021;30:6407–25. https://doi.org/10.1007/s11665-021-06021-7.
[44] Mahmood MA, Chioibasu D, Rehman AU, Mihai S, Popescu AC. Post-processing techniques to enhance the quality of metallic parts produced by additive manufacturing. Metals 2022;12. https://doi.org/10.3390/met12010077.
[45] Maleki E, Bagherifard S, Bandini M, Guagliano M. Surface post-treatments for metal additive manufacturing: progress, challenges, and opportunities. Addit Manuf 2021;37:101619. https://doi.org/10.1016/J.ADDMA.2020.101619.
[46] Khan HM, Karabulut Y, Kitay O, Kaynak Y, Jawahir IS. Influence of the post-processing operations on surface integrity of metal components produced by laser powder bed fusion additive manufacturing: a review. Mach Sci Technol 2020;25:118–76. https://doi.org/10.1080/10910344.2020.1855649.
[47] Behjat A, Shamanian M, Taherizadeh A, Noori M, Lannunziata E, Iuliano L, Saboori A. Enhanced surface properties and bioactivity of additively manufactured 316L stainless steel using different post-treatments. Mater Today Proc 2022. https://doi.org/10.1016/j.matpr.2022.09.019.
[48] A. Naito, O. Takakuwa, H. Soyama, Materials Science and Technology Development of peening technique using recirculating shot accelerated by water jet Development of peening technique using recirculating shot accelerated by water jet, (n.d.). https://doi.org/10.1179/1743284711Y.0000000027.
[49] Prevey PS. X-ray diffraction residual stress techniques. ASM International Mater Charact 1986:380–92. https://doi.org/10.31399/asm.hb.v10.a0001761.
[50] Portella Q, Chemkhi M, Retraint D. Influence of Surface Mechanical Attrition Treatment (SMAT) post-treatment on microstructural, mechanical and tensile behaviour of additive manufactured AISI 316L. Mater Charact 2020;167. https://doi.org/10.1016/j.matchar.2020.110463.
[51] Kumar V, Joshi MD, Pruncu C, Singh I, Hosmani SS. Microstructure and tribological response of selective laser melted AISI 316L stainless steel: the role of severe surface deformation. J Mater Eng Perform 2021;30:5170–83. https://doi.org/10.1007/s11665-021-05730-3.
[52] Maleki E, Unal O, Bandini M, Guagliano M, Bagherifard S. Individual and synergistic effects of thermal and mechanical surface post-treatments on wear and corrosion behavior of laser powder bed fusion AlSi10Mg. J Mater Process Technol 2022;302:117479. https://doi.org/10.1016/j.jmatprotec.2021.117479.
[53] Bagherifard S, Slawik S, Fernández-Pariente I, Pauly C, Mücklich F, Guagliano M. Nanoscale surface modification of AISI 316L stainless steel by severe shot peening. Mater Des 2016;102:68–77. https://doi.org/10.1016/j.matdes.2016.03.162.
[54] Revilla RI, Wouters B, Andreatta F, Lanzutti A, Fedrizzi L, De Graeve I. EIS comparative study and critical Equivalent Electrical Circuit (EEC) analysis of the native oxide layer of additive manufactured and wrought 316L stainless steel. Corrosion Sci 2020;167:108480. https://doi.org/10.1016/j.corsci.2020.108480.
[55] Man C, Dong C, Liu T, Kong D, Wang D, Li X. Applied Surface Science the enhancement of microstructure on the passive and pitting behaviors of selective laser melting 316L SS in simulated body fl uid. Appl Surf Sci 2019;467–468:193–205. https://doi.org/10.1016/j.apsusc.2018.10.150.
[56] Rosa B, Mognol P, Hascoët J. Laser polishing of additive laser manufacturing surfaces. J Laser Appl 2015;27:S29102. https://doi.org/10.2351/1.4906385.
[57] Takakuwa O, Soyama H. Effect of residual stress on the corrosion behavior of austenitic stainless steel. Adv Chem Eng Sci 2015;5:62–71. https://doi.org/10.4236/aces.2015.51007.
[58] Peyre P, Scherpereel X, Berthe L, Carboni C, Fabbro R, Béranger G, Lemaitre C. Surface modifications induced in 316L steel by laser peening and shot-peening. Influence on pitting corrosion resistance. Mater Sci Eng 2000;280:294–302. https://doi.org/10.1016/S0921-5093(99)00698-X.
[59] Vanboven G, Chen W, Rogge R. The role of residual stress in neutral pH stress corrosion cracking of pipeline steels. Part I: pitting and cracking occurrence. Acta Mater 2007;55:29–42. https://doi.org/10.1016/j.actamat.2006.08.037.
[60] Wang K, Chao Q, Annasamy M, Hodgson PD, Thomas S, Birbilis N, Fabijanic D. On the pitting behaviour of laser powder bed fusion prepared 316L stainless steel upon post-processing heat treatments. Corrosion Sci 2022;197:110060. https://doi.org/10.1016/j.corsci.2021.110060.
[61] Kong D, Dong C, Ni X, Zhang L, Yao J, Man C, Cheng X, Xiao K, Li X. Mechanical properties and corrosion behavior of selective laser melted 316L stainless steel after different heat treatment processes. J Mater Sci Technol 2019;35:1499–507. https://doi.org/10.1016/j.jmst.2019.03.003.
[62] Benoit M, Bataillon C, Gwinner B, Miserque F, Orazem ME, Sánchez-Sánchez CM, Tribollet B, Vivier V. Comparison of different methods for measuring the passive film thickness on metals. Electrochim Acta 2016;201:340–7. https://doi.org/10.1016/j.electacta.2015.12.173.
[63] Feng Z, Cheng X, Dong C, Xu L, Li X. Passivity of 316L stainless steel in borate buffer solution studied by Mott–Schottky analysis, atomic absorption spectrometry and X-ray photoelectron spectroscopy. Corrosion Sci 2010;52:3646–53. https://doi.org/10.1016/j.corsci.2010.07.013.
[64] Fattah-alhosseini A. Passivity of AISI 321 stainless steel in 0.5M H2SO4 solution studied by Mott–Schottky analysis in conjunction with the point defect model. Arab J Chem 2016;9:S1342–8. https://doi.org/10.1016/j.arabjc.2012.02.015.
[65] Fattah-alhosseini A, Soltani F, Shirsalimi F, Ezadi B, Attarzadeh N. The semiconducting properties of passive films formed on AISI 316 L and AISI 321 stainless steels: a test of the point defect model (PDM). Corrosion Sci 2011;53:3186–92. https://doi.org/10.1016/j.corsci.2011.05.063.
[66] Saatchi A, Golozar MA, Raeissi K. The passivity of AISI 316L stainless steel in 0.05MH2SO4. 2010. p. 457–61. https://doi.org/10.1007/s10800-009-0016-y.
[67] Jaffré K, Ter-Ovanessian B, Abe H, Mary N, Normand B, Watanabe Y. Effect of mechanical surface treatments on the surface state and passive behavior of 304L stainless steel. Metals 2021;11:1–14. https://doi.org/10.3390/met11010135.
[68] Toor I-H. Mott-Schottky analysis of passive films on Si containing stainless steel alloys. J Electrochem Soc 2011;158:C391. https://doi.org/10.1149/2.083111jes.
[69] Fattah-alhosseini A, Vafaeian S. Comparison of electrochemical behavior between coarse-grained and fine-grained AISI 430 ferritic stainless steel by Mott–Schottky analysis and EIS measurements. J Alloys Compd 2015;639:301–7. https://doi.org/10.1016/j.jallcom.2015.03.142.
[70] Ding J, Zhang L, Lu M, Wang J, Wen Z, Hao W. The electrochemical behaviour of 316L austenitic stainless steel

in Cl− containing environment under different H2S partial pressures. Appl Surf Sci 2014;289:33–41. https://doi.org/10.1016/j.apsusc.2013.10.080.
[71] Macdonald DD. The history of the Point Defect Model for the passive state: a brief review of film growth aspects. Electrochim Acta 2011;56:1761–72. https://doi.org/10.1016/j.electacta.2010.11.005.
[72] BenSalah M, Sabot R, Triki E, Dhouibi L, Refait P, Jeannin M. Passivity of Sanicro28 (UNS N-08028) stainless steel in polluted phosphoric acid at different temperatures studied by electrochemical impedance spectroscopy and Mott–Schottky analysis. Corrosion Sci 2014;86:61–70. https://doi.org/10.1016/j.corsci.2014.04.056.
[73] Hakiki NB, Boudin S, Rondot B, Da Cunha Belo M. The electronic structure of passive films formed on stainless steels. Corrosion Sci 1995;37:1809–22. https://doi.org/10.1016/0010-938X(95)00084-W.
[74] Macdonald DD. The point defect model for the passive state. J Electrochem Soc 1992;139:3434–49. https://doi.org/10.1149/1.2069096.
[75] Atapour M, Wang X, Persson M, Wallinder IO. Corrosion of binder jetting additively manufactured 316L stainless steel of different surface finish corrosion of binder jetting additively manufactured 316L stainless steel of different surface finish. 2020. https://doi.org/10.1149/1945-7111/abb6cd.
[76] Bai L, Jiang K, Gao L. The influence and mechanism of residual stress on the corrosion behavior of welded structures. 21. 2018.
[77] Zakerin N, Morshed-behbahani K. Perspective on the passivity of Ti6Al4V alloy in H 2 SO 4 and NaOH solutions. J Mol Liq 2021;333:115947. https://doi.org/10.1016/j.molliq.2021.115947.
[78] Zakerin N, Najafisayar P. An electrochemical study on the passivity of age hardened Al e Mg e Si alloy. J Mater Res Technol 2020;9:14990–5000. https://doi.org/10.1016/j.jmrt.2020.10.077.
[79] Coelho LB, Kossman S, Mejias A, Noirfalise X, Montagne A, Van Gorp A, Poorteman M, Olivier M-G. Mechanical and corrosion characterization of industrially treated 316L stainless steel surfaces. Surf Coating Technol 2020;382:125175. https://doi.org/10.1016/j.surfcoat.2019.125175.